Estimating Nonstabilizerness Dynamics Without Simulating It

Alessio Paviglianiti,[1,*] Guglielmo Lami,[1,2] Mario Collura,[1,3] and Alessandro Silva[1]

[1] *International School for Advanced Studies (SISSA), via Bonomea 265, 34136 Trieste, Italy*
[2] *Laboratoire de Physique Théorique et Modélisation, CY Cergy Paris Université, CNRS, F-95302 Cergy-Pontoise, France*
[3] *INFN Sezione di Trieste, 34136 Trieste, Italy*

(Received 7 December 2024; revised 18 March 2025; accepted 2 July 2025; published 4 August 2025)

We introduce the iterative Clifford circuit renormalization (ICCR), a novel technique designed to handle the dynamics of nonstabilizerness (also known as quantum magic) in generic quantum circuits composed of Clifford and non-Clifford gates, as well as measurements, extending beyond the reach of pre-existing methods. ICCR iteratively adjusts the starting circuit, transforming it into a Clifford circuit where all elements that can alter the nonstabilizerness, such as measurements or T gates, have been removed. In the process the initial state is renormalized in such a way that the new circuit outputs the same final state as the original one. This approach embeds the complex dynamics of nonstabilizerness in the flow of an effective initial state, enabling the efficient evaluation of stabilizer Renyi entropies and magic nullity while avoiding the need for direct and computationally expensive simulation of the original circuit. The initial state renormalization can be computed explicitly using a matrix-product state approximation that can be systematically improved. We implement the ICCR algorithm to evaluate the nonstabilizerness dynamics for systems of size up to $N = 1000$, in one and more dimensions. We validate our method by comparing it to tensor-network simulations. Finally, we employ the ICCR technique to study measurement-induced magic transitions in monitored circuits without and with T gates.

DOI: 10.1103/msm2-vmg7

I. INTRODUCTION

Investigating the physics of quantum many-body systems using classical simulation is a notoriously challenging task in both condensed matter and statistical physics [1]. The amount of resources needed to represent a many-body quantum state grows exponentially with the number of degrees of freedom involved, thus limiting numerical investigations to small system sizes [2]. Nevertheless, there exist particular classes of quantum states, such as lowly entangled [3–7], Gaussian [8–10], and stabilizer states [11–14], that are simple enough to allow for their efficient simulation on classical devices, yet complex enough to exhibit genuine many-body phenomena, such as quantum criticality and scrambling. The existence of such special states raised the broad problem of classifying and quantifying the complexity of a quantum state, which in parallel has become a useful way to characterize and distinguish different many-body phases.

Currently there is no unique definition of state complexity, as states have many ways to be nontrivial. For N-qubit systems, a possible characterization is given by the so-called nonstabilizerness, also known as *quantum magic* [15–20], which provides a measure of how far a given state is from the class of easy-to-simulate stabilizer states and directly bounds the computational efficiency of its numerical simulation. Multiple measures of magic have been proposed and used to investigate circuit [21–26] and many-body problems [24,27–29]. Despite this progress, the investigation of many-body nonstabilizerness is computationally challenging: not only are nonstabilizer states hard to simulate in the first place, but also the known magic measures are exponentially expensive to evaluate [17,30,31]. While this problem can be mitigated using efficient nonstabilizerness estimation algorithms for matrix product states (MPSs) [27–29,32,33], these limitations hinder the investigation of regimes inaccessible to tensor-network methods, such as very large system sizes, higher dimensionality, or highly entangled states.

In this work, we propose a novel technique, which we name "iterative Clifford circuit renormalization" (ICCR), to address magic efficiently bypassing the aforementioned

*Contact author: paviglianitialessio@gmail.com

Published by the American Physical Society under the terms of the Creative Commons Attribution 4.0 International license. Further distribution of this work must maintain attribution to the author(s) and the published article's title, journal citation, and DOI.

limitations. The method can be applied to states obtained from any given initial state through Clifford circuits doped with nonstabilizer gates and possibly measurements, in principle, in arbitrary dimensionality. The main advantage of our approach is that we avoid entirely evaluation of the evolution generated by the circuit, which is the major computational bottleneck, by iteratively manipulating its geometry and renormalizing the initial state. In practice, we use a simple yet effective approximation method to follow the renormalization flow of the initial state, finding an optimal description as an MPS. Finally, magic can be computed efficiently with a stochastic sampling algorithm [27]. This approach allows for a systematic improvement of the approximation by simply increasing the bond dimension χ of the MPS. We demonstrate that accurate nonstabilizerness estimates can be achieved with relatively low values of χ, much smaller than those required to fully reproduce the state or by conventional MPS methods.

The ICCR algorithm enables the exploration of system sizes up to $N = 1000$. To demonstrate the validity of this technique we investigate several models of monitored quantum circuits, highlighting measurement-induced transitions [34–40] in the dynamics of magic measures tuned by the measurement rate. In detail, we first analyze the problem of a one-dimensional (1D) monitored Clifford circuit where the initial state has extensive nonstabilizerness, and characterize how magic is purified by the measurements. We then expand our investigation to other circuit geometries, exploring the cases of two-dimensional (2D) and long-range Clifford gate structures. At last, we focus on Clifford circuits doped with non-Clifford gates that inject nonstabilizerness throughout the time evolution; in detail, we consider the cases of T-doped monitored Clifford circuits and fully unitary Floquet dynamics.

To validate the accuracy of our method, we investigate the convergence of the nonstabilizerness estimates with χ in the purification dynamics setup. In 1D, we obtain that the overall error scales as approximately χ^{-1}. The convergence is found to be slower in higher dimensions, but still remains efficient in 2D. In addition, we compare our results to exact tensor-network simulations, showing good agreement. Finally, our numerics suggest that even when the magic estimates are not accurate they still provide lower bounds to the exact ones.

The rest of this paper is structured as follows. In Sec. II, we introduce the notion of nonstabilizerness, as well as its measures. Then, Sec. III presents the ICCR algorithm to compute these measures efficiently, providing a step-by-step derivation and a discussion on its performance. We report several examples of application of this formalism in Sec. IV, which introduces the models we consider, our results, an analysis of the error of the approximation, and the benchmark of our method with tensor-network simulations. Finally, we summarize our findings in Sec. V.

II. NONSTABILIZERNESS MEASURES

In this section we briefly review the concept of magic and its measures. First, we define stabilizer states and their main features. We then introduce the nonstabilizerness measures that are relevant for our investigation, namely the stabilizer nullity and the stabilizer Renyi entropies (SREs) [27,30,41–44], commenting on their properties. For convenience, throughout the paper we denote the eigenstates of the Pauli operator $\hat{Z}$ by $|+\rangle$ and $|-\rangle$ (instead of $|0\rangle$ and $|1\rangle$, respectively).

Consider a system of N qubits, and define the N-qubit Pauli group $\mathcal{P}_N = \{\pm 1, \pm i\}\{\hat{\mathbb{1}}, \hat{X}, \hat{Y}, \hat{Z}\}^{\otimes N}$. The class of stabilizer states is the set of states $|\Psi\rangle$ for which there exist N commuting and independent Pauli strings $\hat{g}_i \in \mathcal{P}_N$, $i = 1, \ldots, N$, such that $\hat{g}_i |\Psi\rangle = +|\Psi\rangle$. The operators $\hat{g}_i$ are said to stabilize the state, and they generate the stabilizer group of $|\Psi\rangle$. The knowledge of the N generators completely defines the state. There exists a set of unitary gates, called the Clifford group $\mathcal{C}_N$, that maps stabilizer states into other stabilizer states (and Pauli strings into other Pauli strings). This group is generated by only three elementary gates, namely the Hadamard gate $\hat{H}$, the phase gate $\hat{S}$, and the CNOT gate $\hat{\text{CX}}$.

By applying a non-Clifford gate $\hat{U} \notin \mathcal{C}_N$ to a stabilizer state in general some or all the generators $\hat{g}_i$ will be mapped to $\hat{g}_i' = \hat{U}\hat{g}_i\hat{U}^\dagger \notin \mathcal{P}_N$, thus making the state no longer a stabilizer. The amount of nonstabilizerness of a state can be quantified through different measures. A good measure $\mathcal{M}(|\Psi\rangle)$ should fulfill some properties. First, $\mathcal{M}(|\Psi_{\text{stab}}\rangle) = 0$ if and only if $|\Psi_{\text{stab}}\rangle$ is a stabilizer state, and $\mathcal{M}(|\Psi\rangle) > 0$ otherwise. Second, it must not change under the application of any Clifford operation $\hat{U}_{\text{Cliff}} \in \mathcal{C}_N$, namely, $\mathcal{M}(\hat{U}_{\text{Cliff}}|\Psi\rangle) = \mathcal{M}(|\Psi\rangle)$. Finally, it must be additive for separable states, such that $\mathcal{M}(|\Psi_1\rangle \otimes |\Psi_2\rangle) = \mathcal{M}(|\Psi_1\rangle) + \mathcal{M}(|\Psi_2\rangle)$.

In our analysis we consider two different nonstabilizerness measures. The first measure is the stabilizer nullity ν, which is defined in terms of the stabilizer dimension r. The stabilizer dimension of a state $|\Psi\rangle$ is defined as the maximum integer R for which it is possible to write

$$|\Psi\rangle = \hat{U}_{\text{Cliff}} \left(|+\rangle^{\otimes R} \left| \Phi^{(N-R)} \right\rangle \right), \tag{1}$$

where $\hat{U}_{\text{Cliff}}$ is a suitable Clifford operator, and $\left|\Phi^{(N-R)}\right\rangle$ is a state of $N - R$ qubits. The dimension r coincides with the number of generators $\hat{g}_i \in \mathcal{P}_N$ of the stabilizer group of $|\Psi\rangle$, and it quantifies how many single-qubit stabilizer states it is possible to distill out of $|\Psi\rangle$ using only Clifford operations. The stabilizer nullity is then defined as $\nu = N - r$. We also consider the SREs [30] given by

$$M_n = \frac{1}{1-n} \log_2 \left(\sum_{\hat{P} \in \tilde{\mathcal{P}}_N} \frac{1}{2^N} \langle \Psi | \hat{P} | \Psi \rangle^{2n} \right), \tag{2}$$

where $\tilde{\mathcal{P}}_N = \{\hat{\mathbb{1}}, \hat{X}, \hat{Y}, \hat{Z}\}^{\otimes N}$ is the set of Pauli strings taken without phases. Differently from the nullity, the SREs assume continuous values and they are proper monotones for $n \geq 2$ [42,45]. The nullity is formally given by $\nu = \lim_{n\to\infty}(n-1)M_n$, and can be proven to set an upper bound to M_n [33].

III. ITERATIVE CLIFFORD CIRCUIT RENORMALIZATION

In this section we describe the ICCR technique we developed to study the dynamics of magic. This method can be applied to a wide class of perturbed Clifford circuits where the nonstabilizerness is either introduced in the initial state or directly injected through non-Clifford $\hat{T} = \mathrm{diag}\{1, e^{i\pi/4}\}$ gates. We treat both possibilities in a unified framework, reducing both cases to a nonstabilizer initial state $|\Psi_0\rangle$ evolved with only Clifford operators and computational-basis measurements, as represented schematically in Fig. 1. This is achieved by making use of the so-called T gadget [46,47], which allows us to translate a $\hat{T}$ gate into an equivalent circuit involving a projective measurement and an ancilla qubit prepared in a resource state. In detail, suppose we want to apply a $\hat{T}$ gate to a generic state $|\Psi_S\rangle$ of the system S. We introduce an ancilla qubit A prepared in the resource state $|T_A\rangle = (|+\rangle + e^{i\pi/4}|-\rangle)/\sqrt{2}$. The identity

$$(\hat{T}_S|\Psi_S\rangle)|+_A\rangle = \frac{1}{\sqrt{2}}\frac{\hat{\mathbb{1}} + \hat{Z}_A}{2}\mathrm{C\hat{X}}_{S\to A}\big(|\Psi_S\rangle|T_A\rangle\big) \quad (3)$$

can be easily verified, and it is graphically represented in Fig. 2. Therefore, it is always possible to replace $\hat{T}$ gates by supplementing the system with ancillae and performing Clifford operations and projective measurements.

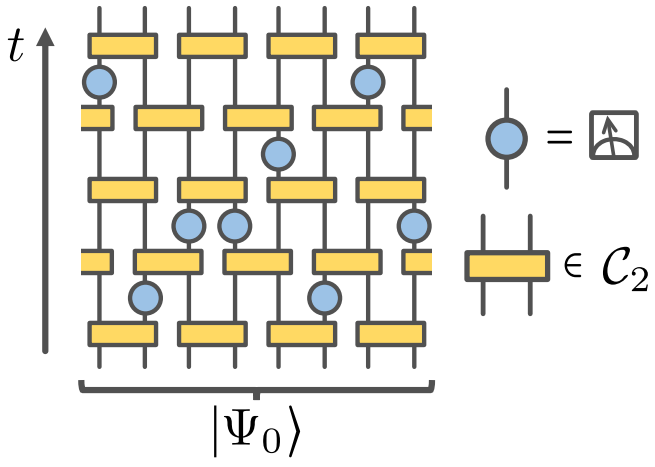


FIG. 1. Example of Clifford circuit with measurements. Measurements of Pauli strings are represented by blue rounded boxes, unitary operators by yellow squared boxes.

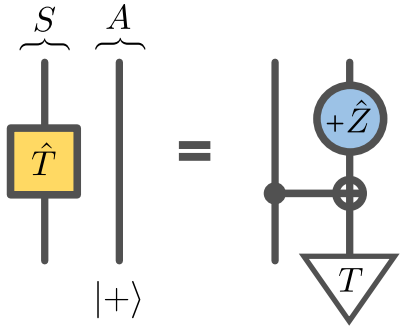


FIG. 2. Graphic representation of the T gadget replacement. The blue circle represents a projective measurement of $\hat{Z}$ with positive outcome, as in Fig. 1.

Below we provide a description of the ICCR method, schematized pictorially in Fig. 3. We start by providing a summary of the technique aimed at clarifying its conceptual procedure and physical intuition. We then explain the details needed for a practical implementation of the method. Finally, we comment on its computational cost and performance.

A. ICCR in a nutshell

The concept underlying the ICCR algorithm is the following. Given a nonstabilizer initial state $|\Psi_0\rangle$ evolved with Clifford unitary gates and projective measurements, we want to obtain a renormalized initial state $|\Psi'\rangle$ and a measurement-free Clifford circuit $\hat{U}'$ such that $\hat{U}'|\Psi'\rangle$ outputs the same state as the original circuit. If successful, this approach enables direct evaluation of magic measures on $|\Psi'\rangle$, bypassing the need of simulating the entire time evolution. The ICCR algorithm performs the task iteratively, i.e., by removing one measurement at a time from the original circuit until none is left.

An iteration of the algorithm proceeds as follows. We consider the initial state $|\Psi_0\rangle$ and the portion of the unitary Clifford circuit $\hat{U}_0$ up to the first projective measurement [as in Fig. 3(a)], which we assume to be of $\hat{Z}_j$ at a certain position j. We swap measurement and unitary gate to obtain an equivalent circuit with a measurement acting directly on $|\Psi_0\rangle$. This transformation can always be accomplished efficiently, since $\hat{U}_0$ is Clifford. The result will yield a projective measurement of a new Pauli string $\hat{P}$ spread across multiple qubits.

The key idea of the ICCR method is to replace the new projector with an appropriate sequence of Clifford unitary gates $\hat{U}'$ acting on a renormalized initial state $|\Psi'\rangle$. In other words, denoting by $\hat{\Pi} = (\hat{\mathbb{1}} + s\hat{P})/2$ the projector associated to the measurement of $\hat{P}$ with outcome $s = \pm$, we want to rewrite

$$\hat{\Pi}|\Psi_0\rangle = \mathcal{N}\hat{U}'|\Psi'\rangle, \quad (4)$$

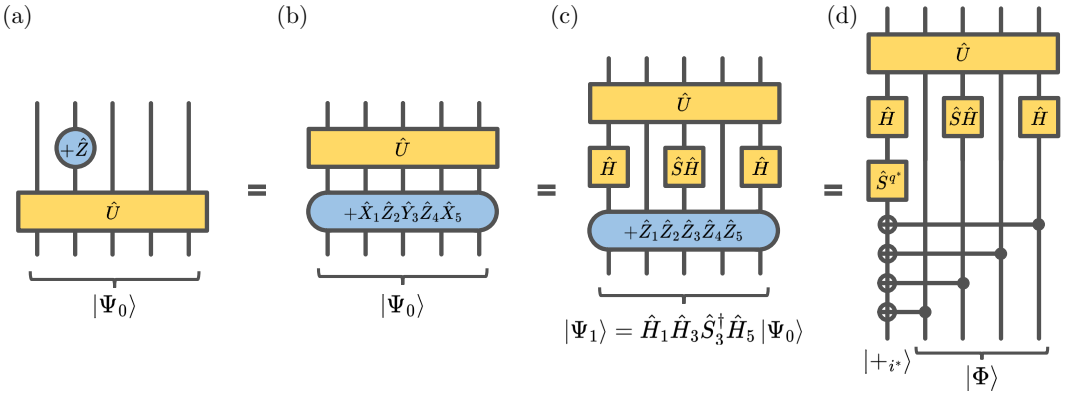


FIG. 3. Schematic representation of the ICCR algorithm. Projectors on Pauli strings are represented by blue rounded boxes, unitary operators by yellow squared boxes. (a) The original circuit involves a unitary Clifford gate followed by a local projector, in this example corresponding to $(\hat{\mathbb{1}} \pm \hat{Z}_2)/2$. (b) The projector is moved through the Clifford gate resulting in a measurement of an extended Pauli string. (c) Single-qubit gates are applied to rotate the new Pauli string into one involving only $\hat{Z}$. (d) The projector is replaced by a cascade of CNOT and single-qubit gates, and the initial state is updated.

where $\mathcal{N}$ is the norm of the left-hand side. A key observation is that, regardless of the outcome s, the projected state obeys the constraint of being an eigenstate of $\hat{P}$, which effectively removes one qubit degree of freedom. This request can be always mimicked by taking $|\Psi'\rangle = |+\rangle\,|\Phi\rangle$ and $\hat{U}'$ as a sequence of CNOT gates entangling $|+\rangle$ with the remaining degrees of freedom [see Fig. 3(d)]. The price to pay is that $|\Phi\rangle$ is in general an unknown complex state. The key approximation would be to determine it variationally by minimizing the distance between $|+\rangle\,|\Phi\rangle$ and $(\hat{U}')^\dagger\hat{\Pi}\,|\Psi_0\rangle$.

B. Description of the implementation

We now explain step by step how to implement the ICCR method. A schematic description can be found in Algorithm 1. The basic iteration of the algorithm can be understood by considering an initial state $|\Psi_0\rangle$ with stabilizer dimension r that is evolved by a Clifford unitary $\hat{U}_0$ followed by a projective measurement of the operator $\hat{Z}_j$, as represented in Fig. 3(a). Taking into account the definition of the stabilizer dimension [cf. Eq. (1)], we can assume without any loss of generality that

$$|\Psi_0\rangle = \bigotimes_{i=1}^{r} |\varphi_i\rangle \left|\Phi^{(N-r)}_{\text{nonstab}}\right\rangle, \tag{5}$$

i.e., the first r spins occupy single-qubit stabilizer states. We would like the projector to act directly on the initial state, so we swap it with the unitary $\hat{U}_0$ by introducing the Pauli string

$$\hat{P} = \hat{U}_0^\dagger \hat{Z}_j \hat{U}_0, \tag{6}$$

which allows us to rewrite

$$\frac{(\hat{\mathbb{1}} \pm \hat{Z}_j)}{2}\hat{U}_0\,|\Psi_0\rangle = \hat{U}_0\frac{(\hat{\mathbb{1}} \pm \hat{P})}{2}\,|\Psi_0\rangle\,, \tag{7}$$

as shown in Fig. 3(b).

The next step to be taken depends on how $\hat{P}$ acts on $|\Psi_0\rangle$, i.e., whether it spreads over many qubits and which ones are involved. First of all, let us check if $\hat{P}$ acts trivially on the stabilizer qubits. Suppose that for $i \le r$ the string contains the operator $\hat{p}_i \in \{\hat{X}_i, \hat{Y}_i, \hat{Z}_i\}$. If $|\varphi_i\rangle$ of Eq. (5) satisfies $\hat{p}_i\,|\varphi_i\rangle = \pm\,|\varphi_i\rangle$, then we can redefine $\hat{P}$ by updating $\hat{p}_i \to \pm\hat{\mathbb{1}}_i$. It might occur that in this process the string $\hat{P}$ is turned into the identity (modulo a sign): this means that the

ALGORITHM 1. ICCR iteration.

Input: the initial state $|\Psi_0\rangle = \bigotimes_{i=1}^{r} |\varphi_i\rangle \left|\Phi^{(N-r)}_{\text{nonstab}}\right\rangle$, a Clifford unitary $\hat{U}_0$ and the measured operator $\hat{Z}_j$.

Compute $\hat{P} = \hat{U}_0^\dagger \hat{Z}_j \hat{U}_0$.
If possible, simplify $\hat{P}$ by checking its action on $|\varphi_i\rangle$.
if $\hat{P}\,|\Psi_0\rangle = \pm\,|\Psi_0\rangle$ **then**
    The measurement leaves the state unchanged, **break**.
end if
Find Cliffords $\hat{q}_i$ such that $\left(\prod_i \hat{q}_i\right)\hat{P}\left(\prod_i \hat{q}_i^\dagger\right) = \prod_{i\in\mathcal{S}} \hat{Z}_i$
Define $|\Psi_1\rangle = \left(\prod_i \hat{q}_i\right)|\Psi_0\rangle$ and $\hat{U}_1 = \hat{U}_0\left(\prod_i \hat{q}_i^\dagger\right)$.
If needed, pick a random outcome s using the Born rule.
Define $(i^*, q^*) = \text{argmax}\,\langle\Psi_1|\,\hat{\pi}_i(q)\,|\Psi_1\rangle$ [see Eq. (13)].
Initialize $|\Psi'\rangle = |\Psi_1\rangle$ and project qubit i^* to $|+_{i^*}\rangle$.
if $i^* > r$ (i^* was nonstabilizer) **then**
    Optimize variationally the nonstabilizer part of $|\Psi'\rangle$.
end if
Define $\hat{U}' = \hat{U}_1\hat{V}$ [see Eq. (15)].

Output: the renormalized initial state $|\Psi'\rangle$ and the equivalent unitary $\hat{U}'$ applied to it.

projective measurement leaves the state unaffected: we can thus drop the measurement from the circuit, and the ICCR step ends here.

In case the action of the projector is nontrivial, we first perform a local change of basis to turn $\hat{P}$ into a string of $\hat{Z}$ Pauli matrices. Let $\mathcal{S}$ be the support of $\hat{P}$, i.e., the set of sites on which it does not act as the identity. We can always find suitable single-qubit Clifford rotations $\hat{q}_i$ such that

$$\left(\prod_{i\in\mathcal{S}}\hat{q}_i\right)\hat{P}\left(\prod_{i\in\mathcal{S}}\hat{q}_i^\dagger\right)=\prod_{i\in\mathcal{S}}\hat{Z}_i. \tag{8}$$

The change of basis requires us to introduce a new initial state

$$|\Psi_1\rangle=\left(\prod_{i\in\mathcal{S}}\hat{q}_i\right)|\Psi_0\rangle=\bigotimes_{i=1}^{r}|\tilde{\varphi}_i\rangle\left|\tilde{\Phi}^{(N-r)}_{\text{nonstab}}\right\rangle \tag{9}$$

and a new unitary $\hat{U}_1=\hat{U}_0\left(\prod_{i\in\mathcal{S}}\hat{q}_i^\dagger\right)$ [see Fig. 3(c)]. Let $s=\pm1$ be the outcome of the measurement. The previous change of basis consists in the rewriting

$$\hat{U}_0\frac{\hat{\mathbb{1}}+s\hat{P}}{2}|\Psi_0\rangle=\hat{U}_1\frac{\hat{\mathbb{1}}+s\prod_{i\in\mathcal{S}}\hat{Z}_i}{2}|\Psi_1\rangle\,. \tag{10}$$

Notice that the outcome is set to $s=+1$ for postselected measurements originated by T gadgets, whereas for other measurements it must be sampled randomly according to the Born rule by evaluating the expectation value $\langle\Psi_1|\prod_{i\in\mathcal{S}}\hat{Z}_i|\Psi_1\rangle$.

The fact that the projective measurement fixes the parity $\prod_{i\in\mathcal{S}}\hat{Z}_i$ to s allows us to represent its action on $|\Psi_1\rangle$ in terms of Clifford unitaries acting on a renormalized state. If we expand $|\Psi_1\rangle$ in the computational basis as

$$|\Psi_1\rangle=\sum_{\sigma_1,\ldots,\sigma_N=\pm1}a_{\sigma_1\ldots\sigma_N}|\sigma_1,\ldots,\sigma_N\rangle\,, \tag{11}$$

the projector destroys all terms in the linear combination that do not fulfill the constraint $\prod_{i\in\mathcal{S}}\sigma_i=s$. The constraint can be thought as reducing by one the free parameters in $\mathcal{S}$. We can mimic the effect of the projective measurement $\prod_{i\in\mathcal{S}}\hat{Z}_i$ with unitary operators by picking a qubit $i^*\in\mathcal{S}$ to be the target qubit of a CNOT gates cascade designed to enforce the parity constraint, as shown in Fig. 3(d). While obviously any qubit in $\mathcal{S}$ can be picked as the target, the optimal choice consists of the qubit of $|\Psi_1\rangle$ that is closest to an eigenstate of $\hat{X}$ or $\hat{Y}$ [48]. Formally, we require that

$$(i^*,q^*)=\arg\max_{i\in\mathcal{S},\,q\in\{0,1,2,3\}}\langle\Psi_1|\,\hat{\pi}_i(q)\,|\Psi_1\rangle\,, \tag{12}$$

where

$$\hat{\pi}_i(q)=|\psi_i(q)\rangle\langle\psi_i(q)| \tag{13}$$

is a projector onto the local state $|\psi_i(q)\rangle=(|+_i\rangle+i^q|-_i\rangle)/\sqrt{2}$ $(q=0,1,2,3)$ that parameterizes $\hat{X},\hat{Y}$ eigenstates on site i. Qubit i^* is the optimal target, whereas q^* determines which eigenstate of $\hat{X}_{i^*}$, $\hat{Y}_{i^*}$ it is closest to. If $\mathcal{S}$ overlaps with the stabilizer qubits we always find $i^*\le r$ [49]. In this case we obtain the identity

$$\frac{\hat{\mathbb{1}}+s\prod_{i\in\mathcal{S}}\hat{Z}_i}{2}|\Psi_1\rangle=\mathcal{N}\hat{V}\left|\Psi'\right\rangle, \tag{14}$$

where $\mathcal{N}$ is the norm of the left-hand side, $\hat{V}$ is the Clifford operator

$$\hat{V}=\hat{S}_{i^*}^{q^*}\left(\prod_{i\in\mathcal{S}\setminus\{i^*\}}\hat{\mathrm{CX}}_{i\to i^*}\right)\hat{X}_{i^*}^{\frac{1-s}{2}}, \tag{15}$$

and the state

$$\left|\Psi'\right\rangle=\bigotimes_{i=1}^{i^*-1}|\tilde{\varphi}_i\rangle\,|+_{i^*}\rangle\bigotimes_{i=i^*+1}^{r}|\tilde{\varphi}_i\rangle\left|\tilde{\Phi}^{(N-r)}_{\text{nonstab}}\right\rangle \tag{16}$$

is equal to $|\Psi_1\rangle$ apart from having qubit i^* set to $|+\rangle$. This result is proved in Appendix A. We successfully replaced the initial circuit with a measurementless one, characterized by the renormalized initial state $\left|\Psi'\right\rangle$ and the new Clifford unitary $\hat{U}'=\hat{U}_1\hat{V}$. Notice that the nonstabilizer part of $\left|\Psi'\right\rangle$ is connected to that of the starting state $|\Psi_0\rangle$ by single-qubit rotations, and thus we conclude that the projective measurement does not modify the magic of the state.

A different scenario unfolds when $i^*>r$, in which case the projective measurement acts only on the nonstabilizer part of the state and impacts it in a nontrivial way. A final form like in Eq. (14) can still be obtained, but $\left|\Psi'\right\rangle$ will grow in complexity as compared to $|\Psi_1\rangle$ (see Appendix A). Even in the special case in which $\left|\Phi^{(N-r)}_{\text{nonstab}}\right\rangle$ of Eq. (5) is a tensor product of single-particle states, the action of the measurement typically results in an entangled renormalized initial state $\left|\Psi'\right\rangle$. The only approximation of this algorithm is made here: to keep the problem tractable, we use a variational approximation of $\left|\Psi'\right\rangle$ and we optimize it within a given class of states to minimize the distance between left- and right-hand sides of Eq. (14). In Sec. IV we implement an MPS approximation, showing that it performs well even with small bond dimension χ (as compared to those needed to explicitly represent the full state). Proceeding in this way, we finally have

$$\left|\Psi'\right\rangle\approx\bigotimes_{i=1}^{r}|\tilde{\varphi}_i\rangle\,|+_{i^*}\rangle\left|\tilde{\Phi}^{(N-r-1)}_{\text{nonstab}}\right\rangle, \tag{17}$$

where the state of nonstabilizer qubits $\left|\tilde{\Phi}^{(N-r-1)}_{\text{nonstab}}\right\rangle$ is obtained variationally. Notice that Eq. (17) is completely

analogous to Eq. (16): the stabilizer states are the same as those of $|\Psi_1\rangle$, and the target qubit is set to $|+_{i^*}\rangle$. Notice however that in this case the stabilizer dimension has been explicitly increased by 1, manifestly changing the magic of the state.

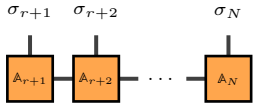
C. Variational approximation of $|\Psi'\rangle$

As mentioned, the ICCR procedure can lead to a growth of complexity of the initial state, which requires approximation of the nonstabilizer part of Eq. (17). When using an MPS ansatz for $|\Psi'\rangle$, the approximation can be performed variationally with a standard MPS compression algorithm. In the following, we discuss in detail how this procedure is implemented.

The only case in which the nonstabilizer part $\left|\tilde{\Phi}^{(N-r)}_{\text{nonstab}}\right\rangle$ of the state $|\Psi_1\rangle$ [cf. Eq. (9)] must be updated is when the support $\mathcal{S}$ is entirely contained in the range $[r+1,\dots,N]$. As a consequence, we can neglect the stabilizer qubits in Eq. (14) and consider only the last $N-r$ ones. First, we assume that $\left|\tilde{\Phi}^{(N-r)}_{\text{nonstab}}\right\rangle$ is given as an MPS

$$\left|\tilde{\Phi}^{(N-r)}_{\text{nonstab}}\right\rangle = \sum_{\sigma_{r+1},\dots,\sigma_N=\pm1} \mathbb{A}^{\sigma_{r+1}}_{r+1}\dots\mathbb{A}^{\sigma_N}_{N}\,|\sigma_{r+1},\dots,\sigma_N\rangle$$

$$= \tag{18}$$



where we introduced standard tensor notation. In the previous equation, each $\mathbb{A}_i$ is a $\chi\times2\times\chi$ tensor, except for the boundary matrices $\mathbb{A}_{r+1}$ and $\mathbb{A}_N$ that are $2\times\chi$ and $\chi\times2$ tensors, respectively. The exact state that we want to approximate is given by

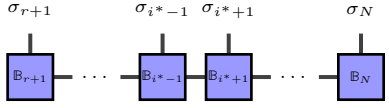
$$|\Psi_{\text{exact}}\rangle = \frac{1}{\mathcal{N}}\frac{\hat{\mathbb{1}}+s\prod_{i\in\mathcal{S}}\hat{Z}_i}{2}\left|\tilde{\Phi}^{(N-r)}_{\text{nonstab}}\right\rangle. \tag{19}$$

The variational ansatz we use is

$$\left|\Psi_{\text{approx}}\right\rangle = \hat{V}\left(|+_{i^*}\rangle\otimes\left|\tilde{\Phi}^{(N-r-1)}_{\text{nonstab}}\right\rangle\right), \tag{20}$$

where

$$\left|\tilde{\Phi}^{(N-r-1)}_{\text{nonstab}}\right\rangle =$$



(21)

is the state appearing in Eq. (17) and it has bond dimension χ as well. Notice site i^* is missing from Eq. (21), and i^*-1 is directly linked to i^*+1.

Our goal is to optimize the choice of $|\beta_i\rangle$ to maximize the overlap

$$\left\langle\Psi_{\text{approx}}\middle|\Psi_{\text{exact}}\right\rangle = \frac{\left(\langle+_{i^*}|\otimes\left\langle\tilde{\Phi}^{(N-r-1)}_{\text{nonstab}}\right|\right)\hat{O}\left|\tilde{\Phi}^{(N-r)}_{\text{nonstab}}\right\rangle}{2\mathcal{N}}, \tag{22}$$

where

$$\hat{O} = \hat{X}_{i^*}^{\frac{1-s}{2}}\left(\prod_{i\in\mathcal{S}\setminus\{i^*\}}\text{CX}_{i\to i^*}\right)(\hat{S}^\dagger_{i^*})^{q^*}\left(\hat{\mathbb{1}}+s\prod_{i\in\mathcal{S}}\hat{Z}_i\right). \tag{23}$$

We notice that the projector $\hat{\mathbb{1}}+s\prod_{i\in\mathcal{S}}\hat{Z}_i$ destroys all computational basis states with parity different from s. Then, the sequence of CNOT gate forces the qubit i^* to the state $|s\rangle$. As a consequence, we can rewrite

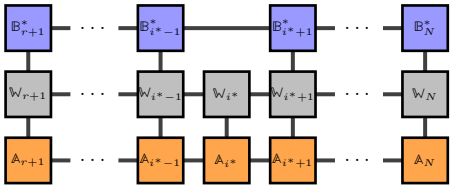
$$\hat{O} = \hat{X}^b_{i^*}\,|s_{i^*}\rangle\left(\langle+_{i^*}|+\langle-_{i^*}|\right)(\hat{S}^\dagger_{i^*})^{q^*}\left(\hat{\mathbb{1}}+s\prod_{i\in\mathcal{S}}\hat{Z}_i\right)$$

$$= |+_{i^*}\rangle\left(\langle+_{i^*}|+i^{-q^*}\langle-_{i^*}|\right)\left(\hat{\mathbb{1}}+s\prod_{i\in\mathcal{S}}\hat{Z}_i\right). \tag{24}$$

The matrix element of Eq. (22) is now given by the tensor contraction

$$\langle\Psi_{\text{approx}}|\Psi_{\text{exact}}\rangle$$

$$= \frac{1}{2\mathcal{N}} \tag{25}$$



where we introduced a matrix-product operator (MPO) defined by

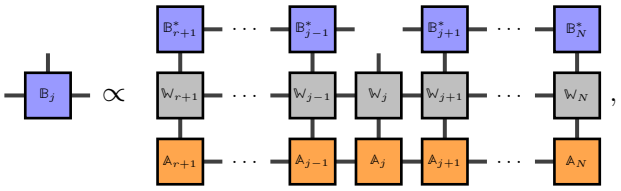
$$\mathbb{W}_i = \begin{pmatrix}\hat{\mathbb{1}} & 0\\ 0 & \hat{M}_i\end{pmatrix} \quad \text{for } i\neq i^*, \tag{26a}$$

$$\mathbb{W}_{i^*} = \begin{pmatrix}\langle+_{i^*}|+\langle-_{i^*}| & 0\\ 0 & s\left(\langle+_{i^*}|-\langle-_{i^*}|\right)\end{pmatrix}, \tag{26b}$$

where $\hat{M}_i=\hat{Z}$ if $i\in\mathcal{S}$ and $\hat{M}_i=\hat{\mathbb{1}}$ otherwise. In the previous equation, the boundary matrices $\mathbb{W}_{r+1}$ and $\mathbb{W}_N$ are understood to be row and column arrays, respectively, to contract correctly.

We set up the variational problem as follows. For each site $j\neq i^*$, we maximize the overlap as a function of $\mathbb{B}_j$ alone fixing all others and imposing the normalization constraint $\left\langle\tilde{\Phi}^{(N-r-1)}_{\text{nonstab}}\middle|\tilde{\Phi}^{(N-r-1)}_{\text{nonstab}}\right\rangle=1$. This is easily done with

standard methods [7] if we assume that $\left|\tilde{\Phi}^{(N-r-1)}_{\text{nonstab}}\right\rangle$ is put in mixed-canonical form centered around site j, in which case the solution of the variational step reads



(27)

where $\mathbb{B}_j$ is determined up to a prefactor that is determined by normalizing the MPS. We then repeat the procedure sweeping through all sites a few times until convergence is reached. Contracting the right-hand side of Eq. (27) has a computational cost that scales as $\mathcal{O}((N-r)\chi^3)$. Since we need to repeat this step multiple times for each site, the overall cost of the iterative optimization scales as $\mathcal{O}((N-r)^2\chi^3)$.

D. Computational cost

Here we discuss the efficiency of each step of the ICCR technique. The overall cost depends on the choice of the variational ansatz: in the following, we assume an MPS representation. In our implementations, we store in memory the stabilizer tableaus of unitary gates. Assuming that at the beginning of the procedure $\hat{U}_0$ consists of a single brick layer of Fig. 1, the cost to compose $N/2$ two-qubit gates is $\mathcal{O}(N^2)$. The evaluation of Eq. (6) is performed in $\mathcal{O}(N)$ operations using stabilizer-state methods [50]. Its simplification by checking how it acts on the states $|\varphi_i\rangle$ is also achieved in at most $\mathcal{O}(N)$ operations. Next, Eq. (9) involves applying $|\mathcal{S}|$ single-qubit unitaries, for a cost that scales as $\mathcal{O}(|\mathcal{S}|) \leq \mathcal{O}(N)$. Evaluating $\langle\Psi_1|\prod_{i\in\mathcal{S}}\hat{Z}_i|\Psi_1\rangle$ and finding i^* and q^* also have the same cost. The evaluation of $\hat{U}'$ amounts to composing $\hat{U}$ with $\mathcal{O}(|\mathcal{S}|)$ one- or two-qubit gates, which costs $\mathcal{O}(N|\mathcal{S}|) \leq \mathcal{O}(N^2)$ operations. Finally, the cost of the optimization required to determine Eq. (17) is $\mathcal{O}((N-r)^2\chi^3) \leq \mathcal{O}(N^2\chi^3)$, as mentioned previously. In summary, the overall maximal cost of the algorithm is $\mathcal{O}(N^2\chi^3)$ per layer and per projective measurement. Assuming a total of M measurements, this brings the overall complexity to $\mathcal{O}(N^2\chi^3 M)$.

For circuits involving a number n_T of T gates a basic way to treat the problem is to replace each of them with a T gadget by introducing n_T ancilla qubits. The total number of qubits to simulate grows, thus increasing the complexity to $\mathcal{O}((N+n_T)^2\chi^3)$ per layer and per projective measurement in the worst-case scenario. While the simulation is still efficient, it can become quite expensive for Clifford circuits doped with many T gates. In Appendix B we show that there is a better way of proceeding that keeps the computational cost at $\mathcal{O}(N^2\chi^3)$. The idea of this alternative approach is that the final state of the ancilla qubit of the T gadget is disentangled from the physical qubits, making it possible to remove its presence from both the effective initial state and the stabilizer tableau of the stored unitary gate. As a consequence, both $|\Psi\rangle$ and $\hat{U}$ are restored to being defined on N qubits.

E. Discussion on the approximation and its generalization

The ICCR algorithm provides a renormalization flow of the initial state $|\Psi\rangle$, which is however expensive to keep track of exactly and is thus approximated by restricting it to a variational class of states. A rather drastic approach is to take the latter as the class of product states, which has the advantage of simplifying the calculation of the SREs of Eq. (2) into a sum of single-qubit SREs due to the additivity property. While this approximation may seem dramatic, our numerical analysis presented in Sec. IV shows that it already captures the qualitative properties of the dynamics of magic. The quality of the approximation is controlled by how close the target qubit i^* is to the eigenstates of $\hat{X}$ and $\hat{Y}$. If the size of the support $\mathcal{S}$ is large the choice of the target is broad and it is more likely to obtain a good approximation. In general, we expect errors to build up as the procedure is iterated, reasonably affecting the performance of the ICCR algorithm at long times.

Beyond this, one can play with the variational class replacing product states with MPSs with fixed bond dimension χ. Though naively analogous, this is very different from performing a full tensor network simulation of the problem, as our goal is still to avoid computing the dynamics. The idea is that while the initial state flow may build up some entanglement, it does not produce as much as the circuit evolution, and thus it can be efficiently captured with a low-χ MPS. The calculation of the SREs becomes more involved, but can still be done efficiently for low enough χ using the perfect sampling technique of Ref. [27], which involves extracting samples of Pauli strings and leveraging the outcomes to form statistical estimators. Unless otherwise specified, we sample 10^3 Pauli strings per SRE measurement. This generalization of the approximation also allows verification of the quality of the estimation by checking the convergence of the SREs as the bond dimension is increased. Indeed, in Sec. IV we show that the accuracy improves with the bond dimension used, and the SREs converge to the exact values as approximately χ^{-1}.

The ICCR step can be effectively viewed as an approach for approximating a generic quantum state using an MPS evolved with a Clifford unitary. This paradigm has been recently established under the name of Clifford enhanced (or augmented) MPSs by Ref. [51] in the context of quantum state designs [52–54], and by Refs. [55–58] from the perspective of increasing the numerical performance of

MPS algorithms. These works suggest a way to further improve the ICCR ansatz by optimizing variationally not only the MPS in Eq. (17), but also the Clifford operator $\hat{V}$ appearing in Eq. (14), rather than assuming the given form of Eq. (15). The implementation of this generalization is left for future studies. In particular, Ref. [58] uses Clifford-augmented MPSs to evaluate the growth of magic, which is closely related to our investigation. However, their focus is on characterizing how much entanglement can be extracted from an MPS using Clifford gates while maintaining an exact state representation. In this work, we instead relax the requirement to capture the state perfectly in order to accurately estimate nonstabilizerness at larger values of N. For this reason, we believe Ref. [58] and our study are complementary.

We expect that the ICCR estimates the stabilizer nullity very accurately, as the latter is insensitive to the specific definition of the nonstabilizer part of the state. Indeed, whether or not the stabilizer dimension increases by 1 depends only on the expression of the Pauli string $\hat{P}$ of Eq. (6) and on the stabilizer qubit states, and not on the details of $\left|\Phi^{(N-r)}_{\text{nonstab}}\right\rangle$. The nullity is also independent of the outcomes of the measurements, which are sampled from an approximation of the initial state [59]. There is, however, a very specific case in which the nullity is not estimated properly. While in our framework the stabilizer dimension can only increase by a unit as a result of a measurement, there exist nonstabilizer states for which it grows by more [60]. These processes are not captured by our framework, making our estimate of ν only an upper bound. Nevertheless, when comparing our method to exact diagonalization we found these instances to be extremely rare [61], making us confident that the ICCR estimates the stabilizer nullity very accurately.

IV. NUMERICAL RESULTS

In this section we present an example of application of the ICCR algorithm, as well as a benchmark of its performance. We consider a model of measurement-induced phase transitions considered in Refs. [34] and [35], which consists of a 1D random Clifford circuit with projective measurements, as schematized in Fig. 1. Differently from these works, here we are interested in the dynamics of magic when the system is initially prepared in a nonstabilizer state $|\Psi_0\rangle$. We consider

$$|\Psi_0\rangle = [\cos(\pi/7)\,|+\rangle + \sin(\pi/7)\,|-\rangle]^{\otimes N}\,, \tag{28}$$

which has extensive nonstabilizerness. Neglecting the measurements, the unitary part of the dynamics forms a brick-wall circuit of depth T, where each two-qubit gate is picked randomly from the two-qubit Clifford group. We assume a ring geometry, so that the first and last qubits are connected by gates. Projective measurements in the Z basis are performed between layers of unitary operators with a density $0 < p < 1$, namely, each spin has a probability p of being measured after being subject to a unitary gate. The measurement outcomes are picked randomly according to the Born rule. As we show below, we observe that the magic features a measurement-induced transition when varying p.

A. Magic purification transition

We employ the ICCR method to study the dynamics of nonstabilizerness in the monitored Clifford circuit described above. This model is known to feature a measurement-induced phase transition [34,35] in both entanglement and mixed-state purification dynamics with the critical point at $p_c \approx 0.16$. To track the renormalization of the initial state, we use MPSs with bond dimension χ as the variational class. Figure 4 shows our numerical results for the densities of second SRE $m_2 = M_2/N$ and nullity ν/N for a system of $N = 1000$ qubits and depth $T = 2N$. We distinguish two phases separated by a critical measurement density p_c that coincides with that observed in previous works. For $p > p_c$, the measurements purify the magic of the system, leaving it in an almost-stabilizer state. In contrast, an extensive nonstabilizerness survives for $p < p_c$, meaning that the state is still nontrivial at times of order $\mathcal{O}(N)$.

As the bond dimension χ is increased, the renormalization of the initial state is followed more accurately, and thus we expect the nonstabilizerness estimates to converge

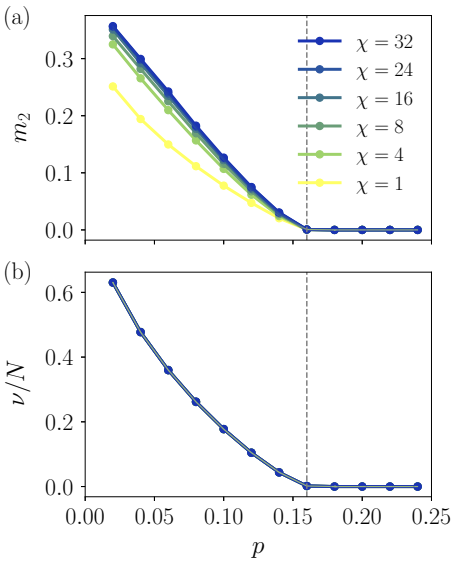


FIG. 4. Long-time magic densities (a) m_2 and (b) ν/N, as functions of the measurement rate p, computed with the ICCR algorithm using different bond dimensions χ. Data for $N = 1000$, $T = 2000$, averaged over 200 realizations. All magic densities vanish for $p > p_c \approx 0.16$, whereas the system still features extensive nonstabilizerness below p_c.

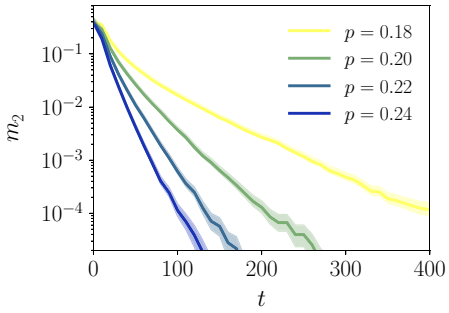


FIG. 5. Dynamics of the second SRE density m_2 for $p > p_c$. Data for $N = 1000$ averaged over 200 realizations. We use $\chi = 32$, although other choices of χ produce qualitatively analogous behavior. The magic relaxes to zero in a finite time with an exponential time dependence.

to the exact results for $\chi \gg 1$. Interestingly, we notice that m_2 grows monotonically as χ is increased, indicating that computing the SRE at finite bond dimension systematically underestimates the true value. This numerical observation suggests that the ICCR method provides lower bounds to the magic measures, even though we were unable to prove it rigorously. In contrast, as argued previously, the stabilizer dimension is independent of χ.

The two phases are better distinguished by looking at how magic evolves as a function of the discrete time t of the circuit. For $p > p_c$, we show in Fig. 5 that the steady state with vanishing nonstabilizerness is reached with an exponential decay profile, with a typical relaxation time that depends on p and we find to be independent of N. In contrast, Fig. 6 shows the case of $p < p_c$, which features very slow dynamics given by $M_2(t) \approx N - A \ln t$ at long times. We observe that the prefactor A of the logarithmic growth is independent of N, and thus it takes an exponentially long time for m_1 to relax to zero. These results are consistent with the numerical investigation presented in Ref. [35], which considers the evolution of the von Neumann entropy $S(\hat{\rho}(t))$ of a density matrix $\hat{\rho}(t)$ initially prepared in $\hat{\rho}(0) = \hat{\mathbb{1}}/2^N$. For $p > p_c$ they observe that the entropy density relaxes to zero in a finite, N-independent time, whereas it remains finite for exponentially long times at small $p < p_c$, precisely as we find for magic measures. Indeed, the authors show that the entropy $S(\hat{\rho})$ actually coincides with the stabilizer nullity ν of $\hat{\rho}$ for the problem they consider. Our investigation thus confirms the findings of Ref. [35], and generalizes it to the case of a pure nonstabilizer initial state.

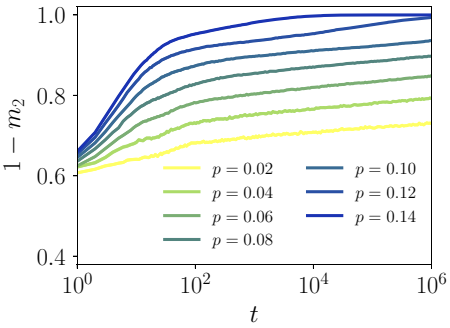


FIG. 6. Dynamics of $1 - m_2$, the complementary of the second SRE density, for $p < p_c$. Data for $N = 140$ averaged over 100 realizations. We use $\chi = 16$, although other choices of χ produce qualitatively analogous behavior. Asymptotically, $1 - m_2$ grows logarithmically in time.

B. Benchmark of the accuracy

We now investigate the rate of convergence of the SRE estimates as the bond dimension χ is increased. This allows us to quantify the bond dimension (and thus the amount of computational resources) needed to achieve a given accuracy. We focus on the phase $p < p_c$, because as shown above in the other region the SRE converges quickly with χ. We consider a system size of $N = 500$, a measurement density $p = 0.1$, and various possible depths $T = 250, 500, 1000$. For each of these, we evaluate $m_2(\chi)$ at different bond dimensions χ. We then estimate the variation $\delta m_2/\delta\chi \approx [m_2(\chi) - m_2(\chi - 5)]/5$, using a step $\delta\chi = 5$ to mitigate numerical error. Figure 7 shows our numerical results. We observe a power-law decay $\delta m_2/\delta\chi \sim \chi^{-2}$. This implies that the cumulative error $m_2(\infty) - m_2(\chi)$ is expected to scale as χ^{-1}, meaning that the bond dimension required to reach a given accuracy ϵ grows as ϵ^{-1}. We also point out that $\delta m_2/\delta\chi > 0$, which further indicates that finite-χ estimates $m_2(\chi)$ are lower bounds of the exact value. To verify the correctness of the ICCR approach, we now compare the values of the stabilizer Renyi entropies obtained using this technique with those obtained through standard tensor-network methods. To this purpose, we perform an MPS simulation without resorting to the state-renormalization techniques

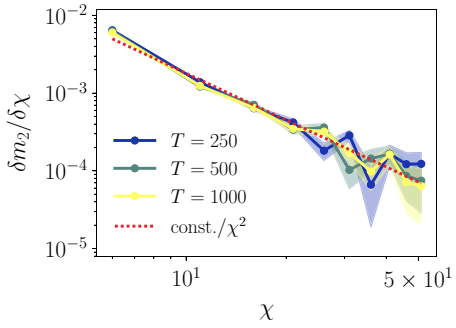


FIG. 7. Estimate of $\delta m_2/\delta\chi$ evaluated at different circuit depths T. Data for $N = 500$ and $p = 0.1$ averaged over 2500 realizations.

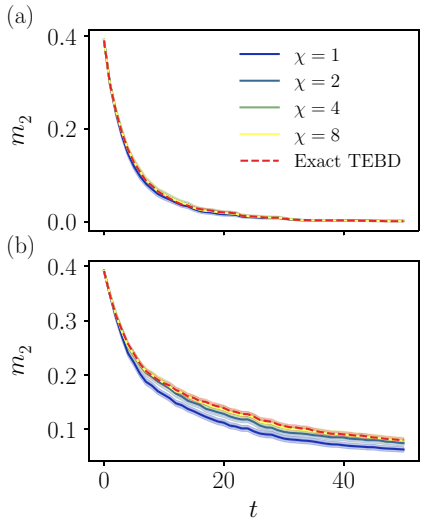


FIG. 8. Average SRE density m_2 computed using the ICCR algorithm with various bond dimensions χ (solid lines) and exact TEBD (dashed red line). Data for $N = 20$ and (a) $p = 0.22$, (b) $p = 0.1$, averaged over 50 random realizations.

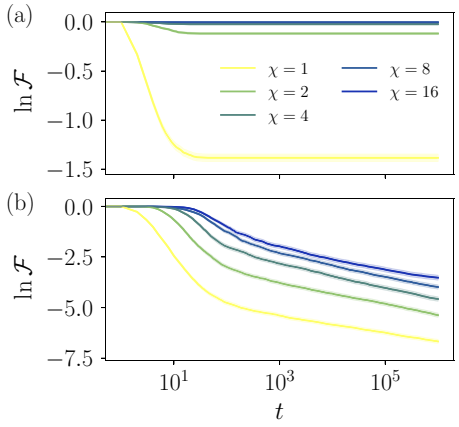


FIG. 9. Dynamics of the logarithmic cumulative fidelity $\ln \mathcal{F}$ in the two phases: (a) $p = 0.22$, and (b) $p = 0.1$. Data for $N = 140$ averaged over 200 realizations.

explained above, simply by contracting the quantum circuit using the time-evolving block-decimation (TEBD) algorithm. We consider a system of size $N = 20$ and study the evolution of the SRE in a circuit of depth $T = 50$ with open-boundary conditions. Importantly, at this system size we are able to follow the state exactly without truncating the TEBD bond dimension. Projective measurements were implemented in the MPS framework using standard techniques [62,63]. The SRE of this simulation is evaluated using the perfect sampling algorithm [27], using a sampling of 10^3 Pauli strings.

In Fig. 8, we present the values of the SRE density m_2 obtained with the ICCR and TEBD approaches [64], for two different values of the projective measurements density $p = 0.1$ and $p = 0.22$. We observe an excellent agreement in the phase $p > p_c$ already with a product-state ansatz ($\chi = 1$), while in the phase $p < p_c$ we require a larger bond dimension to obtain matching values. This shows that the ICCR estimates are unbiased, and they will converge to the exact SRE when using a large enough bond dimension. As observed previously, also in this case the values obtained at small χ appear to lower bound the exact ones.

The different accuracy of the ICCR method in the two phases is reflected qualitatively in the error made by the approximation of Eq. (17). A possible way to quantify it is by keeping track of the overlap between exact and approximate states at each ICCR iteration. Let $|\Psi'_{n,\text{exact}}\rangle$ be the state that solves Eq. (14) at the nth iteration of the ICCR algorithm, and let $|\Psi'_{n,\text{approx}}\rangle$ be its approximation obtained from Eq. (17) (see Sec. III C). We define the squared overlap

$$f_n = |\langle \Psi'_{n,\text{exact}} | \Psi'_{n,\text{approx}} \rangle|^2. \tag{29}$$

Denoting by $M(t)$ the number of ICCR iterations performed up to a given circuit depth t, we introduce the cumulative fidelity

$$\mathcal{F}(t) = \prod_{n=1}^{M(t)} f_n \tag{30}$$

to estimate the drift of the iteratively approximated state from the exact one. In Fig. 9 we show its dynamics for measurement rates p in the two phases. As expected, a larger bond dimension χ implies more variational freedom in the approximation of the state, and as a result the fidelity is higher. The time dependence of $\ln \mathcal{F}$ appears to be logarithmic in time, indicating a power-law decay of the fidelity. For $p = 0.22 > p_c$ and $\chi = 1$, it saturates quickly to a constant $\mathcal{F} \approx 0.25$, which is very large especially considering the system size of $N = 140$; as χ is increased, the fidelity rapidly approaches 1. In contrast, for $p = 0.1 < p_c$ we observe two algebraic regimes: at short times the decay is faster, whereas it features a smaller exponent as longer times. The fidelity decreases much more in this phase, consistently with the worse performance of the ICCR method found in Fig. 8.

The connection between the fidelity and the quality of the SRE estimation is only qualitative, as it clearly emerges from our results that m_2 converges much quicker than $\mathcal{F}$. In other words, while m_2 can be captured quite accurately even using fairly low values of χ, the state itself is not reproduced equally well necessarily, and the fidelity can still be very small due to accumulated errors from the iterative approximation. This is completely reasonable,

because the expectation of capture all properties of a state with a variational approximation that depends on a polynomial amount of parameters is unrealistic. Yet, the more modest goal of computing nonstabilizerness (rather than the full state) can be achieved with limited computational resources.

C. Other circuit geometries

The ICCR algorithm does not depend on the geometry of the Clifford circuit, and can thus be used to study the nonstabilizerness dynamics in more than one dimension. In the following, we extend the previous investigation to other Clifford gate structures, focusing on (i) a 2D and (ii) a long-range geometry. We reproduce analog phase diagrams to the one presented in Fig. 4, and we study the convergence of the SRE as the bond dimension is increased.

First, we consider a 2D geometry where qubits are arranged on a square grid of size $N_x \times N_x$, so that the overall number of sites is $N = N_x^2$. The unitary circuit is obtained by cycling over four layers of (randomly sampled) two-qubit gates, covering (in order) horizontal even neighboring bonds, horizontal odd ones, vertical even ones, and vertical odd ones. We assume periodic boundary conditions. The starting state of the dynamics is still the same as in Eq. (28), and measurements are again applied after each unitary layer with a probability p per site. Figure 10(a) shows our numerical results for the long-time magic density. The transition is qualitatively the same as in the 1D case, but the critical point is shifted to $p_c \approx 0.3$. While accurately quantifying p_c is not the primary aim of our study, we note that this value is consistent with the one reported in Ref. [65], which studied the measurement-induced entanglement transition of 2D random Clifford circuits.

Next, we investigate the SRE convergence in this setting by computing the variation $\delta m_2/\delta\chi$ (as in Sec. IV B). Our results for the 2D system are shown in Fig. 10(b). We still observe a power-law convergence of the SRE, but the decay of $\delta m_2/\delta\chi$ appears to be slightly slower than the 1D case, roughly as approximately $\chi^{-1.7}$ instead of χ^{-2}. This suggests that the convergence of m_2 to its exact value might be slower, yet the approximation can still be improved efficiently with a power-law increase of χ.

We now move to the case of a long-range geometry, in which qubits at arbitrary distances are coupled by Clifford gates. In detail, each layer consists of $N/2$ random unitaries applied on randomly selected pairs of sites. We show the long-time m_2 in Fig. 11(a), where we again observe two distinct purification phases. The critical point $p_c \approx 0.32$ appears to be shifted to an even larger value than the 2D one. This may indicate that magic is scrambled more effectively in higher dimensions, and thus a higher measurement density is required to purify it efficiently.

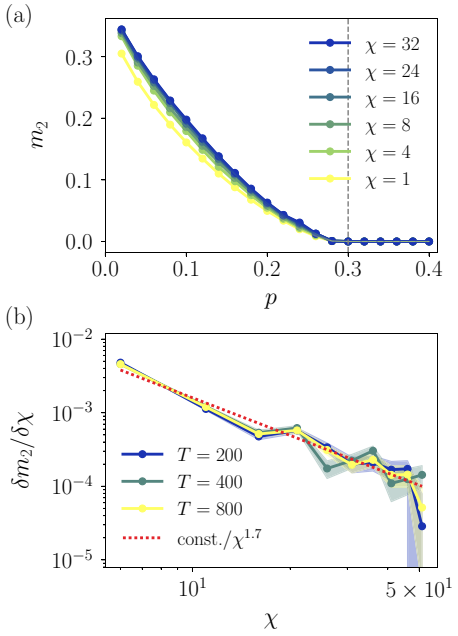


FIG. 10. Long-time m_2 and its convergence upon increasing χ for the 2D geometry, evaluated for $N_x = 20$ ($N = 400$). (a) Dependence of m_2, evaluated at $T = 800$, on p. Data averaged over 200 realizations. (b) Estimate of $\delta m_2/\delta\chi$ evaluated at different circuit depths T. Data for $p = 0.1$ averaged over 2500 realizations.

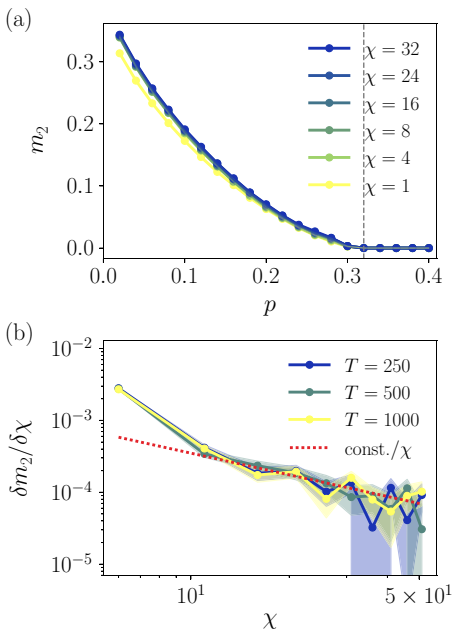


FIG. 11. Long-time m_2 and its convergence upon increasing χ for the long-range geometry, evaluated for $N = 500$. (a) Dependence of m_2, evaluated at $T = 1000$, on p. Data averaged over 200 realizations. (b) Estimate of $\delta m_2/\delta\chi$ evaluated at different circuit depths T. Data for $p = 0.1$ averaged over 2500 realizations.

Finally, we study once again the variation $\delta m_2/\delta\chi$, presented in Fig. 11(b), for the long-range geometry. This time we observe a much slower convergence, which we estimate to be compatible with approximately χ^{-1}. While a precise characterization of the exponent is not possible with the data available, we point out that this result would imply that $m_2(\chi)$ approaches the exact value logarithmically, potentially requiring an exponential scaling of the bond dimension to systematically improve the accuracy. Hence, we expect the ICCR method to perform worse in this scenario, at least when evaluating m_2. This is likely due to our choice to represent the initial state as an MPS, which has an intrinsically one-dimensional structure and struggles to incorporate long-range operations effectively. Hence, while the ICCR method itself is independent of dimensionality, the quality of the approximation of m_2 appears to be affected by it. We remark, however, that the calculation of the nullity is independent of χ, and thus its evaluation (which is enough to obtain the phase diagram) remains feasible also for long-range geometries.

D. Monitored dynamics with T gates

We now discuss the case in which magic is not stored in the initial state, but injected dynamically using T gates throughout the time evolution. In detail, we study a variation of the protocol schematized in Fig. 1, where after each layer of measurements we add an additional layer containing n_T T gates on random sites, and we assume that the system is initially prepared in the stabilizer state $|\Psi_0\rangle = |+\rangle^{\otimes N}$ instead of Eq. (28). This setup has first been considered in Ref. [24], highlighting distinct measurement-induced transitions in entanglement entanglement entropy and nonstabilizerness. This is observed when taking $n_T = \mathcal{O}(1)$, corresponding to an intensive density of T gates per unitary and measurement layer. Here, we employ the ICCR algorithm to enhance the investigation to larger system sizes, corroborating their results on the existence of three phases of magic.

In this protocol, magic starts from zero at $t = 0$, and grows linearly until saturation. We show this in Fig. 12, where we assume a single T gate per layer. The convergence of m_2 upon increase of χ seems much faster as compared to Fig. 4: it appears that only the lowest-level approximation with $\chi = 1$ underestimates the SRE notably, and only for small enough measurement rates. We then proceeded to study the scaling properties of the saturation values reached at $t \gg 1$. In Fig. 13 we present our results for both the long-time M_2 and its density m_2. On the one hand, M_2 manifests scaling behavior below $p_c \approx 0.2$, whereas it is intensive at larger measurement rates. On the other hand, however, Fig. 13(b) indicates that $m_2 \to 0$ as $N \to \infty$ already for $p > p_c' \approx 0.1$. This observation suggests the existence of two separate critical points. At $p < p_c'$, the SRE features a volume law

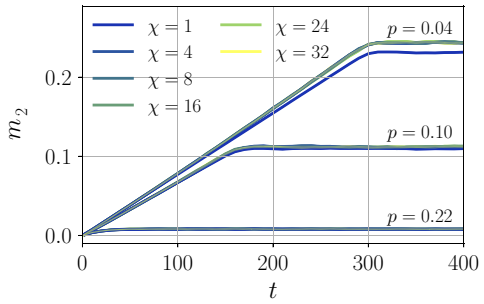


FIG. 12. Dynamics of m_2 starting from a stabilizer product state, assuming $n_T = 1$ T gates per layer, and various measurement rates p. Data for $N = 500$ averaged over 100 realizations. The SRE shows linear growth before saturating. The nonstabilizerness estimates converge very rapidly with χ.

$M_2 \sim N$. For $p_c' < p < p_c$ we instead have a subextensive phase with $M_2 \sim N^\gamma$, where $0 < \gamma < 1$. Finally, the SRE is intensive for $p > p_c$. Besides demonstrating the usefulness of ICCR even in the presence of T gates, our conclusions confirm the results of Ref. [24].

E. Floquet unitary circuit

Lastly, we investigate the performance of ICCR in a fully unitary circuit where an extensive amount of magic is injected at each layer through non-Clifford rotations. We consider a translationally invariant Floquet circuit built by alternating a Clifford layer $\hat{C}$ with a non-Clifford rotation layer $\hat{R}(\varphi)$, such that the time evolution after t steps is given by the unitary operator $(\hat{R}(\varphi)\hat{C})^t$. For the Clifford layer we choose $\hat{C} = (\prod_{i=1}^N \hat{H}_i)(\prod_{i=1}^N \hat{C}Z_{i\to i+1})$, where $\hat{C}Z_{i\to i+1}$ is the controlled Z gate between neighboring qubits, and we impose closed boundary conditions. For the rotation layer we instead use $\hat{R}(\varphi) = \prod_{j=1}^N e^{-i\varphi\hat{Y}_j/2}$, allowing us to tune the amount of injected magic through the parameter φ. These gates can be implemented using

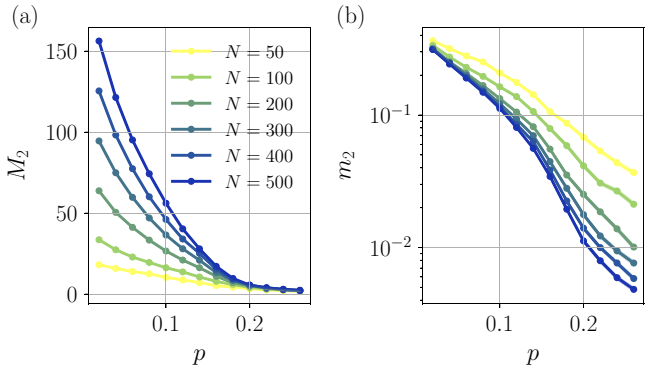


FIG. 13. Steady-state (a) M_2 and (b) m_2 as functions of p and N, starting from a stabilizer product state and assuming $n_T = 1$ T gates per layer. Data for $\chi = 32$ (sufficient for convergence), averaged over 100 realizations.

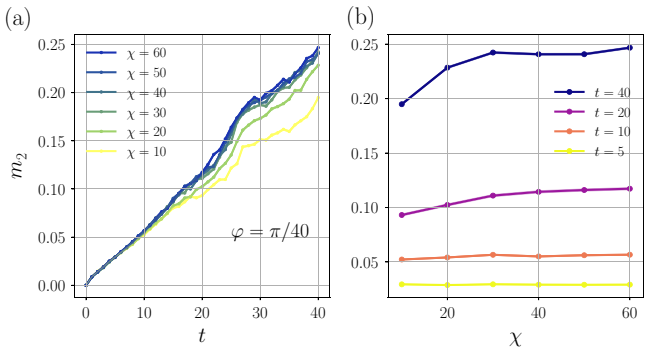


FIG. 14. Dynamics of nonstabilizerness in the Floquet circuit, using $N = 100$ and $\varphi = \pi/40$. (a) Time evolution of $m_2(t)$. (b) m_2 as a function of the bond dimension χ, fixing some choices of t. Here the SRE is evaluated with a sample of 5000 Pauli strings.

a straightforward generalization of the T gadget [66]. Finally, we take $|\Psi_0\rangle = \left(|+\rangle + i\,|-\rangle/\sqrt{2}\right)^{\otimes N}$ as the initial state.

We use the ICCR algorithm to evaluate the SRE m_2 as a function of t, i.e., after each rotation layer. In Fig. 14, we present our results for a small rotation angle $\varphi = \pi/40$, which show an approximately linear growth of nonstabilizerness in time. At early times m_2 is captured accurately even with small bond dimensions, but the quality of the estimates deteriorates as t increases, requiring progressively larger values of χ. This is further illustrated in Fig. 14(b), which shows that m_2 converges to limiting values as χ increases, although the convergence becomes slower at later times

We also consider the case of a large rotation angle $\varphi = \pi/4$, presented in Fig. 15. For this choice, the SRE grows rapidly and appears to saturate at long times. However, analyzing the dependence of m_2 on the bond dimension reveals that convergence is not achieved,

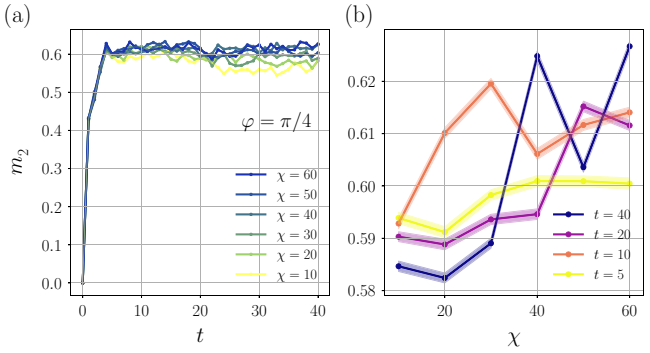


FIG. 15. Dynamics of nonstabilizerness in the Floquet circuit, using $N = 100$ and $\varphi = \pi/4$. (a) Time evolution of $m_2(t)$. (b) m_2 as a function of the bond dimension χ, fixing some choices of t. Here the SRE is evaluated with a sample of 5000 Pauli strings.

indicating that the magic estimates are not quantitatively accurate.

These observations suggest that ICCR may lose accuracy as increasing amounts of nonstabilizerness are injected into the system, eventually making the SRE estimation only qualitative. Indeed, each non-Clifford gate potentially requires a variational optimization step within the algorithm, which inevitably introduces some error. This is consistent with the findings of Ref. [58], which show that magic can no longer be stored by a low-χ Clifford-augmented MPS beyond an extensive threshold number of T gates. Therefore, although the performance of the algorithm should be tested case by case, we generally expect that circuits with an extensive number of non-Clifford unitaries per layer are more challenging to study, and the ICCR method remains quantitatively accurate only at low enough circuit depths.

V. CONCLUSIONS

In this work we propose the new ICCR algorithm to face the challenging problem of evaluating magic in quantum circuits. The main advantage of this technique is that it entirely avoids computing the dynamics of the state explicitly, resulting in a computational cost that scales only polynomially in the number of degrees of freedom. This result is achieved through an iterative manipulation of the structure of the circuit and of the initial state, exploiting the property that Clifford unitary gates preserve the nonstabilizerness. We showcase several applications of ICCR, establishing its versatility to approach a broad class of protocols for systems of up to $N = 1000$ qubits. We start by studying circuits involving projective measurements in one and more dimensions, showing that they exhibit measurement-induced phase transitions in the rate of magic purification. For the 1D and 2D cases, the estimated error on the SRE scales as a power law of the bond dimension χ of the MPS ansatz used to capture the initial state, whereas it appears to be more severe for a long-range circuit connectivity. Nonetheless, we successfully evaluate the phase diagram in all cases, and we observe numerically that results at finite χ lower bound the exact magic values. We then extend our investigation to T-doped monitored Clifford circuits, demonstrating strong ICCR performance and identifying three distinct measurement-induced magic phases. Finally, we address the most challenging case of a Floquet circuit containing an extensive number of non-Clifford rotations per layer, showing that the accuracy of the SRE estimates decreases as more magic gates are applied.

As we have demonstrated, the ICCR method can in principle be applied to any quantum circuit decomposed in terms of Clifford unitaries, non-Clifford gates, and measurements. Nonetheless, we highlight two main scenarios

where we expect the accuracy of the algorithm to be limited. First, as emerged from our study of Clifford circuits with long-range gates, the variational MPS ansatz may not be best suited to study high-dimensional geometries, which feature a potentially inefficient scaling of the computational resources needed to achieve convergence in the SRE estimates. Second, our analysis in Sec. IV E indicates that the ICCR performance worsens in circuits doped with an extensive number of non-Clifford gates per layer, as low-χ MPSs augmented with Clifford gates have been shown to be insufficient to capture the state faithfully [58]. Nevertheless, quantitatively accurate results can still be achieved for shallow enough circuits, and beyond that it may still be possible to extract the qualitative behavior of magic. Moreover, even in these challenging cases the evaluation of the nullity remains efficient, as it is insensitive to the variational approximation.

We believe that ICCR is a powerful and versatile tool to investigate a variety of problems involving nonstabilizerness dynamics, such as those considered in Refs. [22,23,25] on hybrid quantum circuits, at very large system sizes. We expect the ICCR method to reproduce the results of these works with lower computational cost, as we demonstrated by investigating the setup presented in Ref. [24], allowing for an in-depth study of the phase transitions observed. An interesting question left for future studies would be to characterize the performance of ICCR combined with other classes of states for the variational approximation. For instance, while using an MPS still appears to work well for a 2D circuit geometry, a projected entangled pair state (PEPS) ansatz could be more suited and effective. Finally, a relevant question regards the behavior of magic in Clifford circuits with particular structures, instead of random ones, such as gate arrangements corresponding to practically useful quantum computing protocols.

ACKNOWLEDGMENTS

A.P. thanks E. Tirrito, A. Hamma, D. Iannotti, and G. Esposito for useful discussions. This work has been supported by the PNRR MUR project PE0000023-NQSTI, the Quantera project "SuperLink", and the PRIN 2022 (2022R35ZBF) - PE2 - "ManyQLowD". G.L. was partially supported by ANR-22-CPJ1-0021-01.

DATA AVAILABILITY

The data that support the findings of this article are openly available [67].

APPENDIX A: REPLACING A PROJECTOR WITH UNITARY GATES

We prove the identities of Eqs. (14), (15), (16), and we provide the formal exact expression of $|\Psi'\rangle$ of Eq. (17).

First, assume we can find $i^* \leq r$ with $|\tilde{\varphi}_{i^*}\rangle = (|+\rangle + i^{q^*}|-\rangle)/\sqrt{2}$ [cf. Eq. (9)]. Let us perform a computational-base expansion of $|\Psi_1\rangle$. We have

$$\begin{aligned}|\Psi_1\rangle &= \sum_{\sigma_1,\ldots,\sigma_N=\pm1} a_{\sigma_1,\ldots,\sigma_N}|\sigma_1,\ldots,\sigma_N\rangle \\ &= \sum_{\sigma_i\,:\,i\in\mathcal{S}}|\sigma_i\ :\ i\in\mathcal{S}\rangle \sum_{\sigma_i\,:\,i\notin\mathcal{S}} a_{\sigma_1,\ldots,\sigma_N}|\sigma_i\ :\ i\notin\mathcal{S}\rangle \\ &= \sum_{\sigma_i\,:\,i\in\mathcal{S}}|\sigma_i\ :\ i\in\mathcal{S}\rangle\, A_{\{\sigma_i\,:\,i\in\mathcal{S}\}}\left|\psi_{\{\sigma_i\,:\,i\in\mathcal{S}\}}\right\rangle, \end{aligned} \tag{A1}$$

where we isolated the contribution of spins contained in $\mathcal{S}$ by grouping all others in the states $\left|\psi_{\{\sigma_i\,:\,i\in\mathcal{S}\}}\right\rangle$. The latter are normalized to 1, and thus the amplitudes $A_{\{\sigma_i\,:\,i\in\mathcal{S}\}}$ appear in the expansion. Let us introduce a string $\boldsymbol{\sigma} = \{\sigma_i\ :\ i\in\mathcal{S}\setminus\{i^*\}\}$ of length $|\mathcal{S}|-1$ containing all qubits in $\mathcal{S}$ except for the one at i^*. $|\Psi_1\rangle$ can be rewritten compactly as

$$|\Psi_1\rangle = \sum_{\boldsymbol{\sigma}}\sum_{\sigma_{i^*}} A_{\boldsymbol{\sigma},\sigma_{i^*}}|\boldsymbol{\sigma}\rangle\,|\sigma_{i^*}\rangle\left|\psi_{\boldsymbol{\sigma},\sigma_{i^*}}\right\rangle. \tag{A2}$$

Using the fact that qubit i^* is in the known product state $|\tilde{\varphi}_{i^*}\rangle$, the amplitudes factorize as $A_{\boldsymbol{\sigma},\sigma_{i^*}} = \tilde{A}_{\boldsymbol{\sigma}}(i^{q^*})^{\frac{1-\sigma_{i^*}}{2}}/\sqrt{2}$ and the states $\left|\psi_{\boldsymbol{\sigma},\sigma_{i^*}}\right\rangle$ are independent of σ_{i^*}, thus yielding

$$|\Psi_1\rangle = \sum_{\boldsymbol{\sigma}}\tilde{A}_{\boldsymbol{\sigma}}|\boldsymbol{\sigma}\rangle\sum_{\sigma_{i^*}}\frac{(i^{q^*})^{\frac{1-\sigma_{i^*}}{2}}}{\sqrt{2}}|\sigma_{i^*}\rangle\,|\psi_{\boldsymbol{\sigma}}\rangle. \tag{A3}$$

We now evaluate the action of the projector $(\hat{\mathbb{1}} + s\prod_{i\in\mathcal{S}}\hat{Z}_i)/2$ on this state. The projector preserves all components of the superposition satisfying $\prod_{i\in\mathcal{S}}\sigma_i = s$, and destroys all others. As a consequence, defining $\bar{\sigma} = \prod_{i\in\mathcal{S}\setminus\{i^*\}}\sigma_i$, for any given $\boldsymbol{\sigma}$ only states with $\sigma_{i^*} = s\bar{\sigma}$ are not annihilated, yielding

$$\frac{\hat{\mathbb{1}} + s\prod_{i\in\mathcal{S}}\hat{Z}_i}{2}|\Psi_1\rangle = \sum_{\boldsymbol{\sigma}}\tilde{A}_{\boldsymbol{\sigma}}\frac{(i^{q^*})^{\frac{1-s\bar{\sigma}}{2}}}{\sqrt{2}}|\boldsymbol{\sigma}\rangle\,|s\bar{\sigma}\rangle\,|\psi_{\boldsymbol{\sigma}}\rangle. \tag{A4}$$

The state $|s\bar{\sigma}\rangle$ can be achieved by preparing qubit i^* in $|s\rangle$ and controlling it with $|\mathcal{S}|-1$ CNOT gates applied from the spins in $\mathcal{S}\setminus\{i^*\}$. The phase $(i^{q^*})^{\frac{1-s\bar{\sigma}}{2}}$ is reproduced with the gate $\hat{S}_{i^*}^{q^*}$, namely,

$$\begin{aligned}\frac{\hat{\mathbb{1}} + s\prod_{i\in\mathcal{S}}\hat{Z}_i}{2}|\Psi_1\rangle = \frac{1}{\sqrt{2}}\hat{S}_{i^*}^{q^*}\left(\prod_{i\in\mathcal{S}\setminus\{i^*\}}\hat{\mathrm{CX}}_{i\to i^*}\right) \\ \cdot\sum_{\boldsymbol{\sigma}}\tilde{A}_{\boldsymbol{\sigma}}|\boldsymbol{\sigma}\rangle\,|s\rangle\,|\psi_{\boldsymbol{\sigma}}\rangle. \end{aligned} \tag{A5}$$

Notice that the state on the last line of the previous equation is closely related to Eq. (A3), as it differs

only by having $|s\rangle$ instead of $|\tilde{\varphi}_{i^*}\rangle$ on site i^*. Using the identity $|s\rangle = \hat{X}^{\frac{1-s}{2}}|+\rangle$, we finally obtain Eq. (14) with $\mathcal{N} = 1/\sqrt{2}$.

Let us now assume that the target qubit i^* is nonstabilizer. The simplification of Eq. (A2) to Eq. (A3) is no longer possible, the amplitudes $A_{\boldsymbol{\sigma},\sigma_{i^*}}$ do not factorize, and the states $|\psi_{\boldsymbol{\sigma},\sigma_{i^*}}\rangle$ depend also on σ_{i^*}. Acting with the projector we obtain

$$\frac{\hat{\mathbb{1}} + s\prod_{i\in\mathcal{S}}\hat{Z}_i}{2}|\Psi_1\rangle = \sum_{\boldsymbol{\sigma}} A_{\boldsymbol{\sigma},s\bar{\sigma}}\,|\boldsymbol{\sigma}\rangle\,|s\bar{\sigma}\rangle\,|\psi_{\boldsymbol{\sigma},s\bar{\sigma}}\rangle. \tag{A6}$$

Proceeding as in the previous case, we achieve the final form of Eq. (14), but the state $|\Psi'\rangle$ takes the nontrivial form

$$|\Psi'\rangle = \mathcal{N}\sum_{\boldsymbol{\sigma}} A_{\boldsymbol{\sigma},s\bar{\sigma}}\,(i^{-q^*})^{\frac{1-s\bar{\sigma}}{2}}\,|\boldsymbol{\sigma}\rangle\,|+\rangle\,|\psi_{\boldsymbol{\sigma},s\bar{\sigma}}\rangle, \tag{A7}$$

where $\mathcal{N}$ is a normalization prefactor (not necessarily equal to $\sqrt{2}$ as in the previous case). We see explicitly that the stabilizer dimension increases by one, as the initially nonstabilizer target qubit i^* is brought to $|+\rangle$. Instead, the state of the other qubits increases in complexity, because in general it develops entanglement even when starting from a product state configuration.

APPENDIX B: OPTIMAL WAY TO TREAT *T* GATES

The ICCR algorithm can be applied to circuits doped with T gates using the T gadgets introduced in Sec. III. The straightforward implementation of this method requires the introduction of n_T ancilla qubits, where n_T is the number of T gates in the circuit, which increases the computational cost of the simulation. We now show a better strategy to proceed that requires only a single ancilla qubit that can be reused for all T gates.

Consider an initial state $|\Psi_S\rangle$ evolved with a Clifford circuit and then with a single T gate. Using the T gadget replacement, we can reformulate the evolution as in Fig. 3(a), where now the initial state $|\Psi\rangle = |\Psi_S\rangle\,|T_A\rangle$ is the product of the N-physical-qubit state $|\Psi_S\rangle$ and the ancilla-qubit state $|T_A\rangle$, and the projector acts on the ancilla. We implement the ICCR algorithm, which approximates the end-circuit state as

$$|\Psi_f\rangle = \hat{U}'\,|\Psi'\rangle. \tag{B1}$$

We can make some exact statements on both $|\Psi'\rangle$ and $|\Psi_f\rangle$. The renormalized initial state $|\Psi'\rangle$ contains at least one stabilizer qubit (i.e., the target qubit i^*) in the factorized state $|+\rangle$ as in Fig. 3(d), and can thus be written as $|\Psi'\rangle = |\Phi\rangle\,|+_{i^*}\rangle$. Then, the final state can always be written as $|\Psi_f\rangle = |\Psi_{f,S}\rangle\,|+_A\rangle$ because the projector disentangles the ancilla from the physical qubits. If we swap the ancilla with the qubit i^* by defining $|\Psi'_S\rangle\,|+_A\rangle = \text{SW}\hat{\text{AP}}_{i^*\leftrightarrow A}|\Psi'\rangle$, where SWAP is the (Clifford) SWAP gate, we have

$$|\Psi_{f,S}\rangle\,|+\rangle_A = \hat{U}'\,\text{SW}\hat{\text{AP}}_{i^*\leftrightarrow A}(|\Psi'_S\rangle\,|+_A\rangle) = \hat{U}''(|\Psi'_S\rangle\,|+_A\rangle). \tag{B2}$$

We see that the Clifford unitary $\hat{U}''$ leaves the ancilla in the state $|+\rangle$. This means that there must exist a Clifford operator $\hat{W}_S$ acting only on S such that $\hat{U}''(|\Psi'_S\rangle\,|+_A\rangle) = (\hat{W}_S|\Psi'_S\rangle)\,|+_A\rangle$. Notice however that in general $\hat{U}'' \neq \hat{W}_S\hat{\mathbb{1}}_A$. We now show how to determine $\hat{W}_S$.

Our goal is to find a new Clifford unitary $\hat{\tilde{U}}$ such that it acts in the same way as $\hat{U}''$ and at the same time has both $\hat{Z}_A$ and $\hat{X}_A$ in its stabilizer set. Hence, we require

$$\hat{\tilde{U}}(|\Psi'_S\rangle\,|+_A\rangle) = \hat{U}''(|\Psi'_S\rangle\,|+_A\rangle), \tag{B3}$$

$$\hat{\tilde{U}}^\dagger\hat{Z}_A\hat{\tilde{U}} = \pm\hat{Z}_A, \tag{B4}$$

and

$$\hat{\tilde{U}}^\dagger\hat{X}_A\hat{\tilde{U}} = \pm\hat{X}_A. \tag{B5}$$

Notice that the sign $\pm$ of Eq. (B5) does not necessarily need to be the same as that of Eq. (B4). Since $\hat{U}''$ does not change the state $|+\rangle$ of the ancilla, one may think that $\hat{Z}_A$ already belongs to its stabilizer set. However, this is not necessarily the case, as the unitary gate $\hat{U}''$ may also generate Pauli operators that act trivially on the initial state. In general, we have

$$(\hat{U}'')^\dagger\hat{Z}_A\hat{U}'' = \pm\left(\prod_{i=1}^{r}\hat{P}_i\right)\hat{Z}_A, \tag{B6}$$

where the string of $\hat{P}_i \in \{\hat{\mathbb{1}}_i, \hat{X}_i, \hat{Y}_i, \hat{Z}_i\}$ acts only on the stabilizer qubits and must satisfy $\left(\prod_{i=1}^{r}\hat{P}_i\right)|\Psi_S\rangle = \pm|\Psi_S\rangle$. For each i, we define

$$\hat{C}[\hat{P}_i] = \begin{cases} \hat{\mathbb{1}} & \text{if } \hat{P}_i = \hat{\mathbb{1}}_i, \\ \hat{C}X_{A\to i} & \text{if } \hat{P}_i = \hat{X}_i, \\ \hat{C}Y_{A\to i} & \text{if } \hat{P}_i = \hat{Y}_i, \\ \hat{C}Z_{A\to i} & \text{if } \hat{P}_i = \hat{Z}_i, \end{cases} \tag{B7}$$

where $\hat{C}Y_{A\to i}$ and $\hat{C}Z_{A\to i}$ are, respectively, the controlled Y and Z gates that use the ancilla as reference and i as target. We introduce

$$\hat{U}''' = \hat{U}''\prod_{i=1}^{r}\hat{C}[\hat{P}_i], \tag{B8}$$

which acts on the state in the same way as $\hat{U}''$ due to the definition of $\hat{C}[\hat{P}_i]$. Moreover, it easily checked that $\hat{Z}_A$ is in the stabilizer set of $\hat{U}'''$.

Regarding $\hat{X}_A$, in general the unitary gate will map it to a complicated string

$$(\hat{U}''')^\dagger \hat{X}_A \hat{U}''' = \pm \left(\prod_{i=1}^{N} \hat{P}'_i \right) \hat{P}'_A, \tag{B9}$$

where $\hat{P}'_i \in \{\hat{\mathbb{1}}_i, \hat{X}_i, \hat{Y}_i, \hat{Z}_i\}$ and $\hat{P}'_A \in \{\hat{X}_A, \hat{Y}_A\}$. Notice that $\hat{P}'_A$ cannot be neither $\hat{\mathbb{1}}_A$ nor $\hat{Z}_A$ because $\left[(\hat{U}''')^\dagger \hat{Z}_A \hat{U}''' (\hat{U}''')^\dagger \hat{X}_A \hat{U}'''\right] = (\hat{U}''')^\dagger \left[\hat{Z}_A \hat{X}_A\right] \hat{U}''' \neq 0$. Similarly to how we proceeded before, we introduce

$$\hat{\tilde{U}} = \hat{U}''' \left(\prod_{i=1}^{N} \hat{C}[\hat{P}'_i] \right) \hat{u}_A, \tag{B10}$$

where $\hat{u}_A = \hat{S}_A$ if $\hat{P}'_A = \hat{Y}_A$ and $\hat{u}_A = \hat{\mathbb{1}}_A$ otherwise. It is easily checked that Eqs. (B3), (B4), and (B5) are satisfied. In particular, the last two imply that the gate $\hat{\tilde{U}}$ is unable to entangle the system with the ancilla for all initial states. We thus conclude that $\hat{\tilde{U}} = \hat{W}_S \hat{Q}_A$, where $\hat{Q}_A$ is a single-qubit gate that acts as a phase on $|+_A\rangle$. Finally, the stabilizer tableau of $\hat{W}_S$ is obtained by dropping the rows and columns of the tableau of $\hat{\tilde{U}}$ corresponding to the ancilla qubit, yielding the final identity

$$\left|\Psi_{f,S}\right\rangle = \hat{W}_S \left|\Psi'_S\right\rangle \tag{B11}$$

for the physical qubits alone.

[1] R. P. Feynman, Simulating physics with computers, Int. J. Theor. Phys. **21**, 467 (1982).

[2] W. Kohn, Nobel Lecture: Electronic structure of matter—wave functions and density functionals, Rev. Mod. Phys. **71**, 1253 (1999).

[3] P. Silvi, F. Tschirsich, M. Gerster, J. Jünemann, D. Jaschke, M. Rizzi, and S. Montangero, The tensor networks anthology: Simulation techniques for many-body quantum lattice systems, SciPost Phys. Lect. Notes, 8 (2019).

[4] J. Biamonte, Lectures on quantum tensor networks, ArXiv:1912.10049.

[5] G. Vidal, Efficient simulation of one-dimensional quantum many-body systems, Phys. Rev. Lett. **93**, 040502 (2004).

[6] M. B. Hastings, An area law for one-dimensional quantum systems, J. Stat. Mech.: Theory Exp. **2007**, P08024 (2007).

[7] U. Schollwöck, The density-matrix renormalization group in the age of matrix product states, Ann. Phys. **326**, 96 (2011).

[8] B. M. Terhal and D. P. DiVincenzo, Classical simulation of noninteracting-Fermion quantum circuits, Phys. Rev. A **65**, 032325 (2002).

[9] R. Jozsa and A. Miyake, Matchgates and classical simulation of quantum circuits, Proc. R. Soc. A: Math. Phys. Eng. Sci. **464**, 3089 (2008).

[10] J. Surace and L. Tagliacozzo, Fermionic Gaussian states: an introduction to numerical approaches, SciPost Phys. Lect. Notes, 54 (2022).

[11] D. Gottesman, Stabilizer codes and quantum error correction, Arxiv:quant-ph/9705052.

[12] D. Gottesman, Theory of fault-tolerant quantum computation, Phys. Rev. A **57**, 127 (1998).

[13] D. Gottesman, The Heisenberg representation of quantum computers, ArXiv:quant-ph/9807006.

[14] S. Aaronson and D. Gottesman, Improved simulation of stabilizer circuits, Phys. Rev. A **70**, 052328 (2004).

[15] S. Bravyi and A. Kitaev, Universal quantum computation with ideal Clifford gates and noisy ancillas, Phys. Rev. A **71**, 022316 (2005).

[16] J. R. Seddon, B. Regula, H. Pashayan, Y. Ouyang, and E. T. Campbell, Quantifying quantum speedups: improved classical simulation from tighter magic monotones, PRX Quantum **2**, 010345 (2021).

[17] V. Veitch, S. A. H. Mousavian, D. Gottesman, and J. Emerson, The resource theory of stabilizer quantum computation, New J. Phys. **16**, 013009 (2014).

[18] M. Howard and E. Campbell, Application of a resource theory for magic states to fault-tolerant quantum computing, Phys. Rev. Lett. **118**, 090501 (2017).

[19] Z.-W. Liu and A. Winter, Many-body quantum magic, PRX Quantum **3**, 020333 (2022).

[20] L. Leone, S. F. E. Oliviero, Y. Zhou, and A. Hamma, Quantum chaos is quantum, Quantum **5**, 453 (2021).

[21] S. F. E. Oliviero, L. Leone, A. Hamma, and S. Lloyd, Measuring magic on a quantum processor, Npj Quantum Inf. **8**, 148 (2022).

[22] P. Niroula, C. D. White, Q. Wang, S. Johri, D. Zhu, C. Monroe, C. Noel, and M. J. Gullans, Phase transition in magic with random quantum circuits, Nat. Phys. **20**, 1786 (2024).

[23] X. Turkeshi and P. Sierant, Error-resilience phase transitions in encoding-decoding quantum circuits, Phys. Rev. Lett. **132**, 140401 (2024).

[24] G. E. Fux, E. Tirrito, M. Dalmonte, and R. Fazio, Entanglement – nonstabilizerness separation in hybrid quantum circuits, Phys. Rev. Res. **6**, L042030 (2024).

[25] M. Bejan, C. McLauchlan, and B. Béri, Dynamical magic transitions in monitored Clifford+T circuits, PRX Quantum **5**, 030332 (2024).

[26] A. F. Mello, G. Lami, and M. Collura, Retrieving nonstabilizerness with neural networks, Phys. Rev. A **111**, 012440 (2025).

[27] G. Lami and M. Collura, Nonstabilizerness via perfect Pauli sampling of matrix product states, Phys. Rev. Lett. **131**, 180401 (2023).

[28] G. Lami and M. Collura, Unveiling the stabilizer group of a matrix product state, Phys. Rev. Lett. **133**, 010602 (2024).

[29] P. S. Tarabunga, E. Tirrito, T. Chanda, and M. Dalmonte, Many-body magic via Pauli-Markov chains—from criticality to gauge theories, PRX Quantum **4**, 040317 (2023).

[30] L. Leone, S. F. E. Oliviero, and A. Hamma, Stabilizer Renyi entropy, Phys. Rev. Lett. **128**, 050402 (2022).

[31] T. Haug and M. Kim, Scalable measures of magic resource for quantum computers, PRX Quantum **4**, 010301 (2023).

[32] T. Haug and L. Piroli, Quantifying nonstabilizerness of matrix product states, Phys. Rev. B **107**, 035148 (2023).

[33] P. S. Tarabunga, E. Tirrito, M. C. Bañuls, and M. Dalmonte, Nonstabilizerness via matrix product states in the Pauli basis, Phys. Rev. Lett. **133**, 010601 (2024).

[34] B. Skinner, J. Ruhman, and A. Nahum, Measurement-induced phase transitions in the dynamics of entanglement, Phys. Rev. X **9**, 031009 (2019).

[35] M. J. Gullans and D. A. Huse, Dynamical purification phase transition induced by quantum measurements, Phys. Rev. X **10**, 041020 (2020).

[36] X. Turkeshi, R. Fazio, and M. Dalmonte, Measurement-induced criticality in $(2+1)$-dimensional hybrid quantum circuits, Phys. Rev. B **102**, 014315 (2020).

[37] A. Nahum, S. Roy, B. Skinner, and J. Ruhman, Measurement and entanglement phase transitions in all-to-all quantum circuits, on quantum trees, and in Landau-Ginsburg theory, PRX Quantum **2**, 010352 (2021).

[38] A. Zabalo, M. J. Gullans, J. H. Wilson, S. Gopalakrishnan, D. A. Huse, and J. H. Pixley, Critical properties of the measurement-induced transition in random quantum circuits, Phys. Rev. B **101**, 060301 (2020).

[39] A. Paviglianiti and A. Silva, Multipartite entanglement in the measurement-induced phase transition of the quantum Ising chain, Phys. Rev. B **108**, 184302 (2023).

[40] P. Sierant, M. Schirò, M. Lewenstein, and X. Turkeshi, Measurement-induced phase transitions in $(d+1)$-dimensional stabilizer circuits, Phys. Rev. B **106**, 214316 (2022).

[41] S. F. E. Oliviero, L. Leone, and A. Hamma, Magic-state resource theory for the ground state of the transverse-field Ising model, Phys. Rev. A **106**, 042426 (2022).

[42] T. Haug and L. Piroli, Stabilizer entropies and nonstabilizerness monotones, Quantum **7**, 1092 (2023).

[43] E. Tirrito, P. S. Tarabunga, G. Lami, T. Chanda, L. Leone, S. F. E. Oliviero, M. Dalmonte, M. Collura, and A. Hamma, Quantifying nonstabilizerness through entanglement spectrum flatness, Phys. Rev. A **109**, L040401 (2024).

[44] D. Rattacaso, L. Leone, S. F. E. Oliviero, and A. Hamma, Stabilizer entropy dynamics after a quantum quench, Phys. Rev. A **108**, 042407 (2023).

[45] L. Leone and L. Bittel, Stabilizer entropies are monotones for magic-state resource theory, Phys. Rev. A **110**, L040403 (2024).

[46] S. Bravyi and D. Gosset, Improved classical simulation of quantum circuits dominated by Clifford gates, Phys. Rev. Lett. **116**, 250501 (2016).

[47] X. Zhou, D. W. Leung, and I. L. Chuang, Methodology for quantum logic gate construction, Phys. Rev. A **62**, 052316 (2000).

[48] As we shall see later, replacing the measurement with unitary gates can require a redefinition of the initial state of the circuit, and possibly an increase in its complexity. If the target qubit is in an eigenstate of $\hat{X}$ or $\hat{Y}$ the redefinition is trivial, and it does not bear any growth of complexity.

[49] We previously removed from $\mathcal{S}$ all sites $i \leq r$ corresponding to eigenstates of $\hat{Z}$. Hence, any $i \in \mathcal{S}$ with $i \leq r$ must correspond to an eigenstate of $\hat{X}$ or $\hat{Y}$.

[50] C. Gidney, Stim: a fast stabilizer circuit simulator, Quantum **5**, 497 (2021).

[51] G. Lami, T. Haug, and J. D. Nardis, Quantum state designs with Clifford-enhanced matrix product states, PRX Quantum **6**, 010345 (2025).

[52] M. Ippoliti and W. W. Ho, Solvable model of deep thermalization with distinct design times, Quantum **6**, 886 (2022).

[53] D. Gross, K. Audenaert, and J. Eisert, Evenly distributed unitaries: on the structure of unitary designs, J. Math. Phys. **48**, 052104 (2007).

[54] A. A. Mele, Introduction to Haar measure tools in quantum information: a beginner's tutorial, Quantum **8**, 1340 (2024).

[55] X. Qian, J. Huang, and M. Qin, Augmenting density matrix renormalization group with Clifford circuits, Phys. Rev. Lett. **133**, 190402 (2024).

[56] A. F. Mello, A. Santini, and M. Collura, Hybrid stabilizer matrix product operator, Phys. Rev. Lett. **133**, 150604 (2024).

[57] J. Huang, X. Qian, and M. Qin, Non-stabilizerness entanglement entropy: a measure of hardness in the classical simulation of quantum many-body systems, ArXiv:2409.16895.

[58] G. E. Fux, B. Béri, R. Fazio, and E. Tirrito, Disentangling unitary dynamics with classically simulable quantum circuits, ArXiv:2410.09001.

[59] The difference between the two possible measurement outcomes only amounts to the presence or absence of an $\hat{X}$ gate in Eq. (15). This gate, being a π rotation, can at most affect the outcomes s of the following iterations.

[60] M. Beverland, E. Campbell, M. Howard, and V. Kliuchnikov, Lower bounds on the non-Clifford resources for quantum computations, Quantum Sci. Technol. **5**, 035009 (2020).

[61] These events are rare in the sense that they typically require a fine tuning of the properties of the state to occur. For instance, consider the state $|\Psi_0\rangle = |T\rangle^{\otimes 2}$ with stabilizer dimension $r = 0$, and perform a measurement of the Pauli operator $\hat{Z}_1\hat{Z}_2$. For both possible outcomes, the final state will be stabilizer, thus having $r = 2$. However, if $|\Psi_0\rangle$ is slightly perturbed, for instance by a small rotation generated by $\hat{Z}_1$, then both postmeasurement states will have $r = 1$. Hence, it is indeed possible that r grows by more than a unit, but this requires a careful and fine-tuned choice of the state.

[62] E. M. Stoudenmire and S. R. White, Minimally entangled typical thermal state algorithms, New J. Phys. **12**, 055026 (2010).

[63] A. J. Ferris and G. Vidal, Perfect sampling with unitary tensor networks, Phys. Rev. B **85**, 165146 (2012).

[64] For this comparison, we adopted the same trajectories (i.e., the same choices of Clifford gates and measurement outcomes) in the two methods.

[65] O. Lunt, M. Szyniszewski, and A. Pal, Measurement-induced criticality and entanglement clusters: a study of one-dimensional and two-dimensional Clifford circuits, Phys. Rev. B **104**, 155111 (2021).

[66] First, we use Clifford gates to rewrite the Y rotation in terms of a Z rotation as $e^{-i\varphi\hat{Y}/2} = \hat{H}\hat{S}^\dagger e^{-i\varphi\hat{Z}/2}\hat{S}\hat{H}$. Next, the Z rotation by the angle φ is implemented analogously to the T gate, using the ancilla resource state $|\varphi_A\rangle = (|+\rangle + e^{-i\varphi/2}|-\rangle)/\sqrt{2}$ in place of $|T_A\rangle$ in Eq. (3).

[67] A. Paviglianiti, G. Lami, M. Collura, and A. Silva, Data for: estimating non-stabilizerness dynamics without simulating it (2025).